

mm. The aluminum plate areas where the TEG-enabled GFRP unit was placed were included in the geometrical mesh, which were necessary for the temperature difference to be created. The abovementioned finite-difference procedure approximately created roughly 700000 nodes with 100000 elements. The discretized simulated model of the TEG-enabled GFRP unit is illustrated in Figure S2a. The superthin epoxy resin which interconnects the consecutive layers and the semiconductors, was simulated as a material with electrical conductivity $\sim 10^{-7} \text{ S}\cdot\text{m}^{-1}$ and thermal conductivity $\sim 10^7 \text{ W}\cdot\text{m}^{-1}\cdot\text{K}^{-1}$, to provide essential thermal energy flow while avoiding unwanted electric transit across interfaces, simulating in this way the operating conditions of the GFRP-GTEG unit. Figure S2b illustrates a model geometry view along with the applied boundary conditions, where the electrical potential difference translated to open circuit voltage is given between the first n-type and the last p-type semiconductor elements. The “bottom” side aluminum base of the GFRP-GTEG unit functioned as the “cold” and was maintained at 25°C . The device’s “top” portion was in touch with the aluminum “hot-plate”. Each of the first semiconductor of the GFRP-GTEG unit had been grounded with a potential difference of 0 V, to guide the flow of the electric energy of current created by the ΔT . The physical requirements listed here function as the applied boundary conditions for modeling simulation analysis and were imposed to the FEA solver. The properties of the material used for the GFRP-TEG device modeling simulation, i.e. electrical conductivity, Seebeck coefficient, thermal conductivity, were determined by the experimental values of the current study in order to compare the measured and simulated data directly.

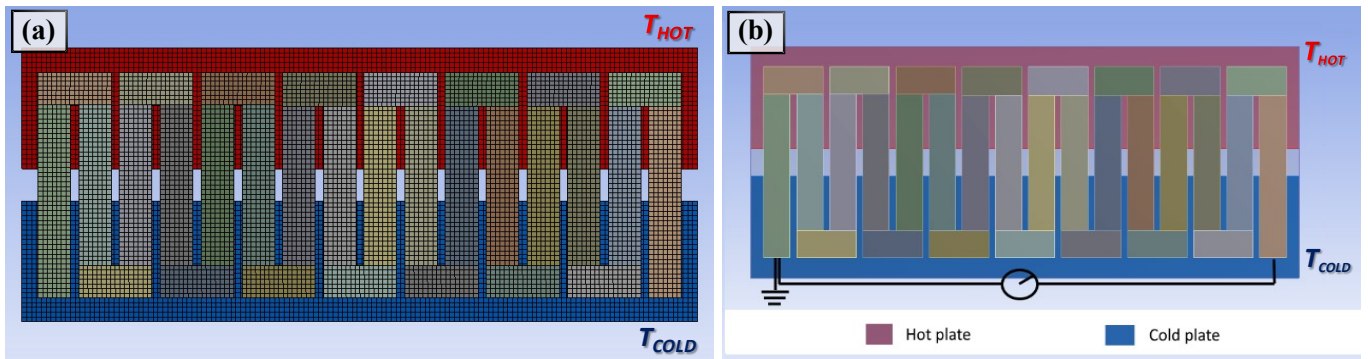


Figure S2. (a) Discretized structural TEG-enabled GFRP unit hosting 16 semiconductor elements (8 p-type and 8 n-type in alternating sequence) along with the GF substrate (in light blue background color). (b) The model geometry view along with the applied boundary conditions. The ground point is shown on the down left corner. Hot and cold aluminum plate regions are located on the top and bottom sides of the GFRP-GTEG unit, respectively.

Figure S3 shows the simulation results of the electrical potential difference (ΔV) between the first and last semiconductor of the GFRP-GTEG module calculated for an 8 p/n- pair unit.

A rough estimation invoking the Seebeck phenomenon $|\Delta V(T)| = |S \Delta T|$ (ignoring actual temperature variations, as well as thermal energy transmission between layers) may be utilized to compare the experimental Seebeck values of n- and p-type materials employed in the GFRP-GTEG unit with the extracted Seebeck coefficient $|S_{\text{sim}}| = 425.00 \mu\text{V/K}$ from the simulated data.

Because of the GFRP-GTEG unit comprises 8 n- and p-type thermoelements, the Seebeck value for one p-/n- pair was $53.13 \mu\text{V}/\text{K}$, which is very similar to the calculated experimental value of the pair $|S_{n, p \text{ pair}}^{\text{exp}}| = |S_{n\text{-type}}| + |S_{p\text{-type}}| = (25 + 28) \mu\text{V}/\text{K} = 53 \mu\text{V}/\text{K}$.

Despite the thermal and electrical losses included in the experimental approach, the output voltages estimated from the FEA were in good accordance with the measured values. The TEG device consisting of 29 GFRP-GTEG units/232 p-/n- pairs of semiconductor thermoelements produced the maximum output voltage with the numerical predicted value $\Delta V_{\text{sim}} = 1.23 \text{ V}$ being in reasonable agreement to the experimentally measured $\Delta V_{\text{exp}} = 1.01 \text{ V}$ at a $\Delta T = 100 \text{ }^\circ\text{C}$. The reliability and robustness of the present simulation approach were validated by the agreement between simulated results and experimental measurements.

The TEG-enabled structural device consisted of one or multiple GFRP-GTEG units, resulting in a total Ohmic resistance of $R_{\text{TEG}} = N_{\text{unit}} R_{\text{GFRP-GTEG.unit}}$ where N_{unit} is the number of GFRP-GTEG units and $R_{\text{GFRP-GTEG.unit}} = 40.96 \text{ Ohm}$. The maximum power transfer theorem, often known as Jacobi's law, asserts that the resistance of the load must match the resistance of the source as measured from its output terminals in order to acquire maximum external power from a source with a finite internal resistance. The exact maximum power P_{max} might be easily determined utilizing the maximum power transfer theorem, and is equal to: $P_{\text{max}} = (V_{\text{TEG}}^2)/(4 \cdot R_{\text{TEG}})$, where V_{TEG} is the measured voltage (V), of the manufactured device.

Following the early stages of the experimental TEG device development, additional numerical models were used to capture the functional features of the aforementioned devices consisting of GFRP-GTEG units configured in a stacking sequence. The resulting layered device can be used in the cases where the interconnection of multiple GFRP-GTEG units in linear fashion is prohibited due to plane dimension restrictions. The voltage output and consequently the power generation of each individual GFRP -GTEG unit depends strongly on the temperature difference ΔT . The stacking procedure of interconnected GFRP -GTEG units differentiates the resulting multilayer TEG device since only the first layer and consequently the first GFRP-GTEG unit experiences the temperature difference ΔT dictated by the aluminum ‘hot’ and ‘cold’ heat baths. Heat losses and geometry induced heat conduction along the different layers have an immediate impact on the output electrical characteristics of the layered device. The presence of air on the sides of GFRP-GTEG units and the additional thermal resistances that each unit introduces to the actual heat conduction were considered in the layered device modeling procedure.

Figure S4 shows the generated $V_{\text{OC}} = 549 \text{ mV}$ and the $I_{\text{SC}} = 473 \mu\text{A}$ of the GFRP-GTEG at $\Delta T = 50\text{K}$ ($T_{\text{C}} = 25^\circ\text{C}$), noting an $R_{\text{TEG}} = 1128 \Omega$ and a $P_{\text{MAX}} = 69 \mu\text{W}$.

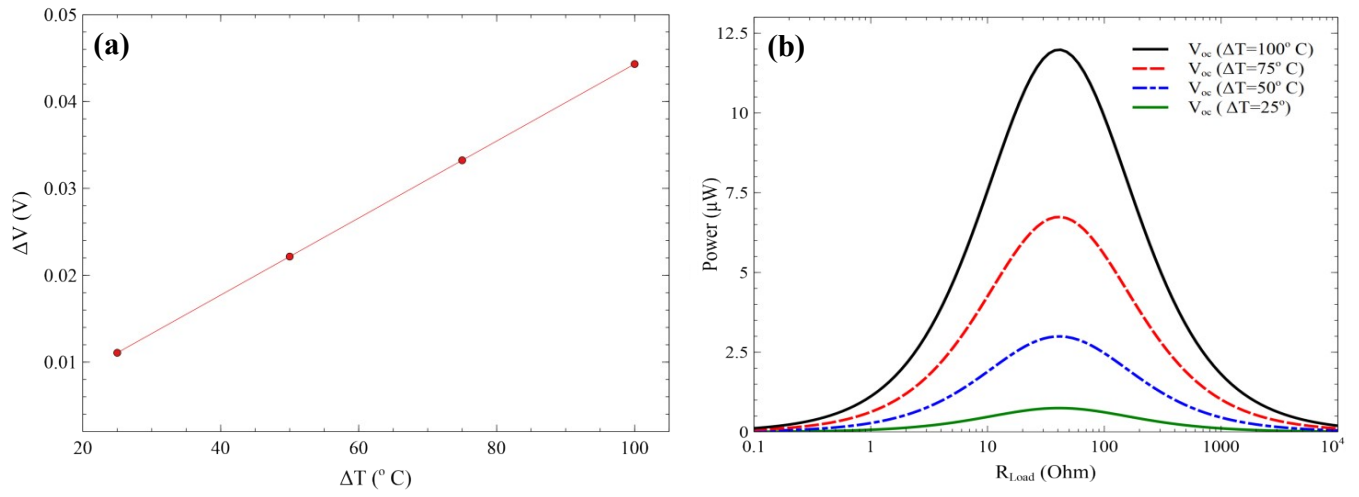


Figure S3. Simulation results of voltage difference ΔV (a) for an 8 p-/n- pair GFRP-GTEG unit exposed to temperature difference of $\Delta T=100^{\circ}\text{C}$. (b) The calculated electric power generation by the GFRP-GTEG unit at different temperature differences $\Delta T=25, 50, 75, 100^{\circ}\text{C}$.

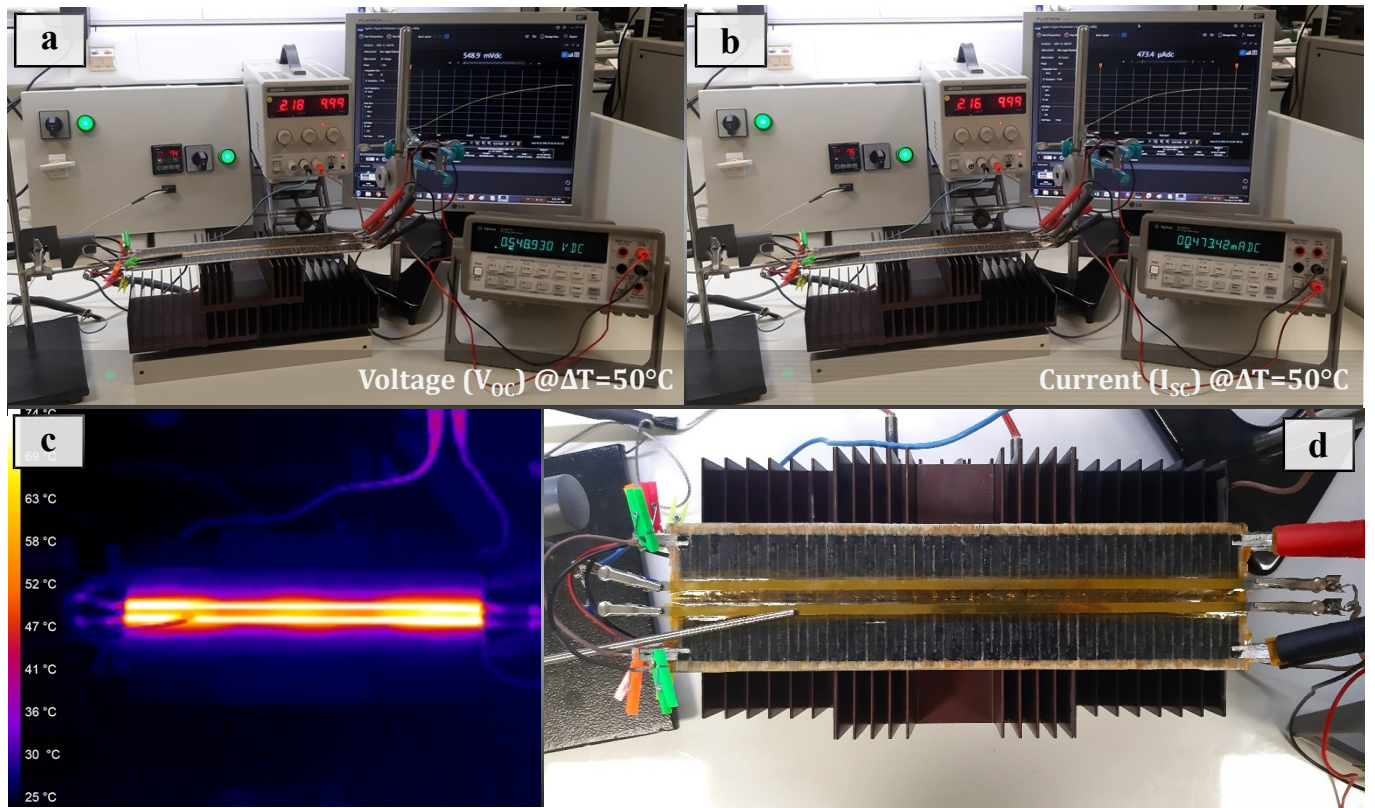


Figure S4. GFRP-GTEG-device performance at $\Delta T:50\text{K}$: (a) the generated open-circuit voltage (V_{oc}) and, (b) the short-circuit current (I_{sc}). (c) Thermal image of the testing performance and (d) the thermoelectric power measurement set-up.

Figure S5 illustrates the stability of the p- and n-type resin impregnated thermoelements in air @ $\Delta T=100\text{K}$ ($T_c=25^\circ\text{C}$). Figure S6 depicts the Raman measurements of the PEDOT:PSS film.

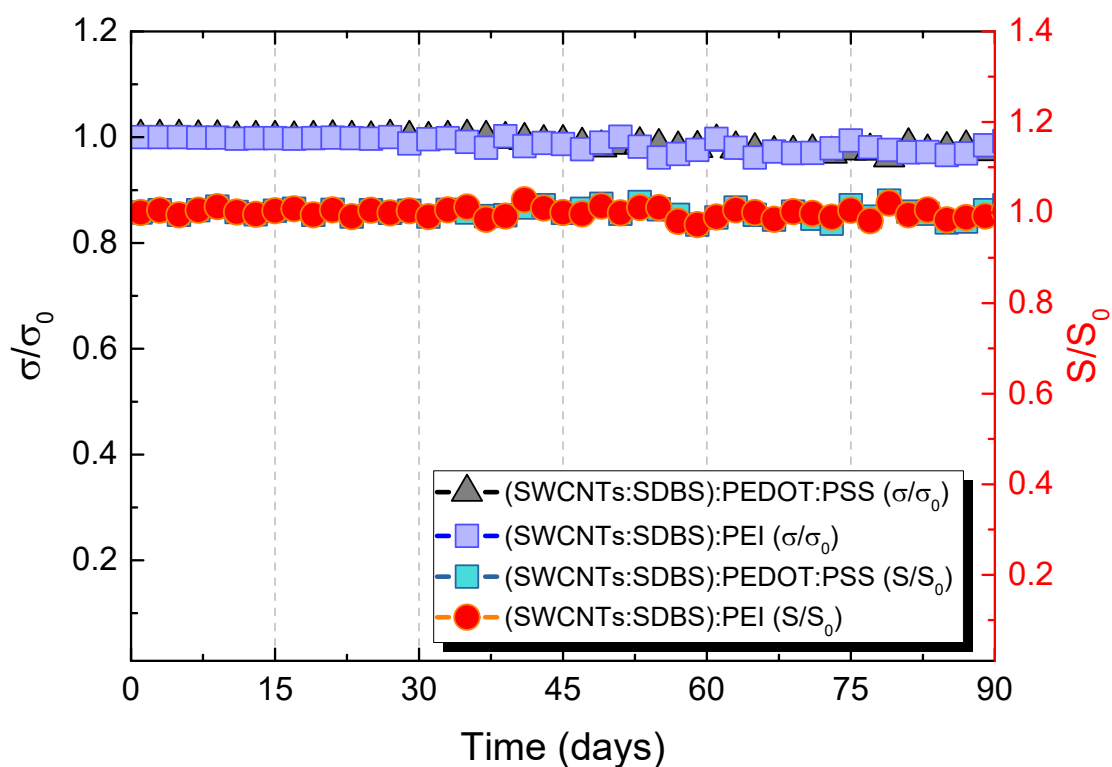


Figure S5. The long-term stability of dominant n- and p-type resin impregnated materials in air @ $\Delta T=100\text{K}$.

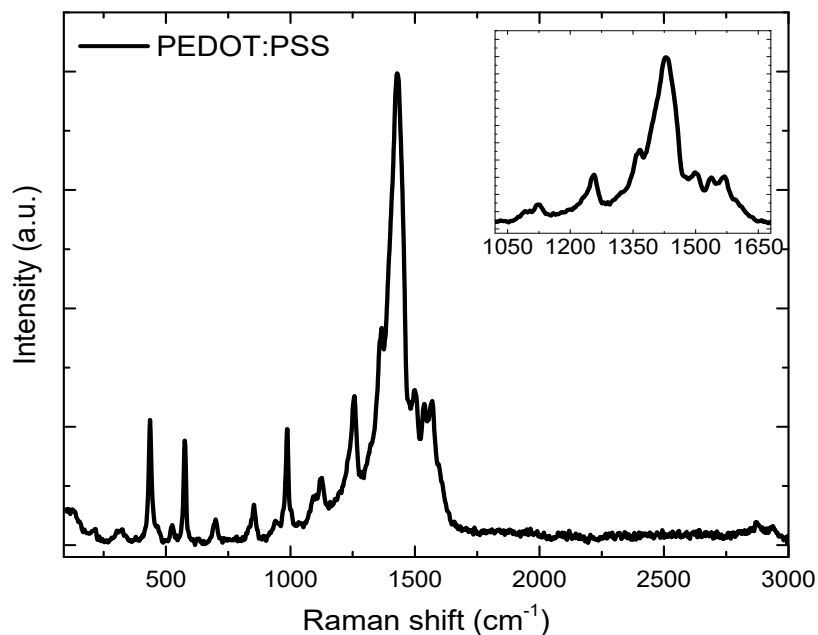


Figure S6. Raman measurements of PEDOT:PSS film.

Figure S7 illustrates the time needed for ALD-EH4295 to charge, utilizing the power generated from the GFRP-GTEG module to power up a LED at $\Delta T=10\text{K}$.

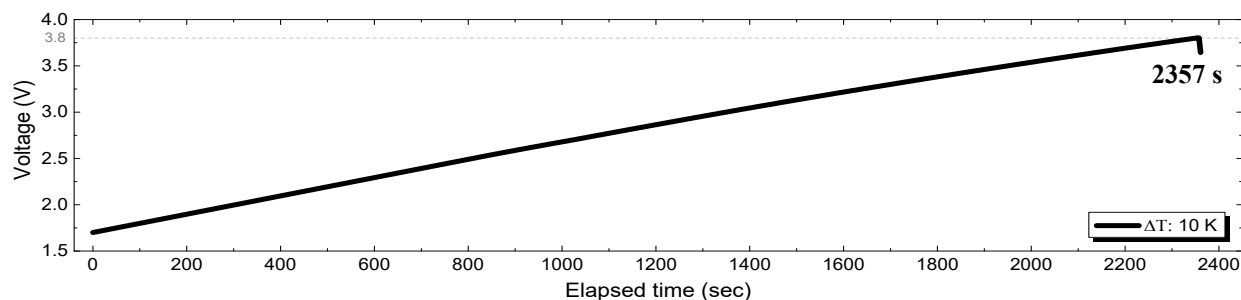


Figure S7. The time needed for ALD-EH4295 to charge utilizing the power generated from the GFRP-GTEG module to power up a LED @ $\Delta T=10\text{K}$.

Figure S8 illustrates a comparison between the (a) power factors of the p- and n-type carbon-based TE materials and (b) the voltage and the power output generated between our structural TEG device with values from relevant studies reported in literature.

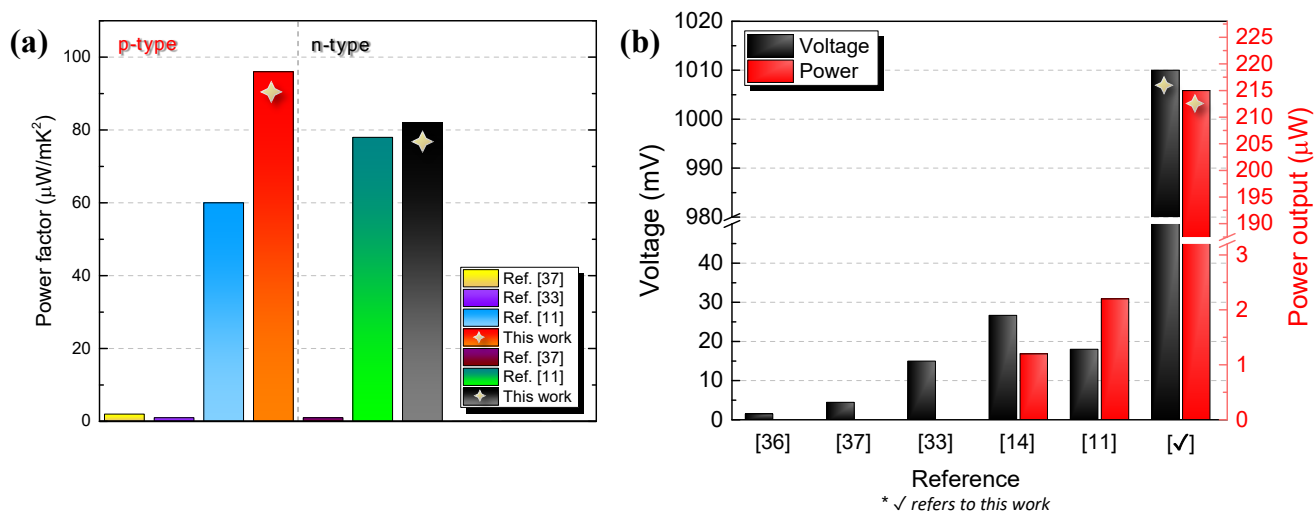


Figure S8. Comparison between the (a) power factors of the p- and n-type carbon-based TE materials and (b) the voltage and the power output generated between our structural TEG device with values from relevant studies reported in literature